Available online at www.sciencedirect.com

jmr&t
Journal of Materials Research and Technology

journal homepage: www.elsevier.com/locate/jmrt

Original Article

Microstructure and phase evolution of functionally graded multi-materials of Ni–Ti alloy fabricated by laser powder bed fusion process

Phuangphaga Daram [a,*], *Takanobu Hiroto* [b], *Makoto Watanabe* [a]

[a] *Research Center for Structural Materials, National Institute for Materials Science, 1-2-1 Sengen, Tsukuba, Ibaraki, 305-0047, Japan*

[b] *Research Network and Facility Services Division, Materials Analysis Station, National Institute for Materials Science, 1-2-1 Sengen, Tsukuba, Ibaraki, 305-0047, Japan*

ARTICLE INFO

Article history:
Received 31 October 2022
Accepted 20 February 2023
Available online 1 March 2023

Keywords:
Laser powder bed fusion process
Functionally graded materials
Ni-Ti alloy
Microstructure
Compositional gradient

ABSTRACT

The layer-by-layer laser powder bed fusion (L-PBF) process was applied to fabricate functionally graded multi-materials (FGMs) of nickel-titanium alloy. The FGMs Ni–Ti alloy was built with composition transitioning from pure Ni incrementally graded to pure Ti by different composition gradients. The microstructure, chemical composition, and phase evolution were characterized using SEM, EDS, XRD, and EBSD along the build direction. By varying the proportions of Ni and Ti, the microstructure and phases were changed gradually across the build direction. Several phase transformations, γ-Ni → NiTi B2 + intermetallic phases → α-Ti, appeared through the compositional gradient. Cracks were found in the gradient zone, and the results were explained in terms of the various phases present. The potential to accomplish such a completely deposited FGMs Ni–Ti alloy and considerable changes in composition are made possible by a new strategy to make innovative FGMs Ni–Ti alloys together with 3D components using L-PBF additive manufacturing.

1. Introduction

Multi-materials have various beneficial properties, which differ and sometimes vary in different parts of a particular component such as in the automotive, energy industries, aerospace, biomaterials, and other industries [1]. To fabricate multi-materials in the single manufacturing, it is possible to create functionally graded materials (FGMs) with improved material interface characteristics. The most common type of metallic FGMs is from pure material A to pure material B with directly, gradient path, and intermediate section methods [2]. Additive manufacturing (AM) has the potential to extend the design of complex structures in efficiently to save production time and the cost of the materials used. One of the highest-potentials AM techniques is the laser powder bed fusion (L-PBF) process, a rapidly developing layer-by-layer technique with high densification and complex parts using metal, alloy,

* Corresponding author.
E-mail address: daram.phuangphaga@nims.go.jp (P. Daram).

https://doi.org/10.1016/j.jmrt.2023.02.151

ceramic, or composite materials [3,4]. The L-PBF system with two powder feeders is possible for material and product design, such as by varying powders at given ratios in the formation of an FGMs. For most situations, the L-PBF process is used in the production of FGMs with discrete gradients. Tan et al. [5] reported the interfacial characterization of Cu joined with W directly via the layer-by-layer L-PBF process. They found a lack of fusion and small cracks at interface between W and Cu. In addition, an interfacial W–Cu bonding with an inter-diffusion region of 50–80 μm was presented, which led to good metallurgical bonding between W and Cu. Similar to W–Cu FGMs, a steel-bronze multi-material was fabricated by using different parameters of the L-PBF process reported by Chen et al. [6]. A hole and cracking at the interface of steel and bronze are related to the interfacial process parameters, which are the main factors affecting in bonding failure. Many works obviously reported that a mismatch and the coefficient of thermal expansion of two different materials, is caused mainly by cracking at the interface [5–7]. FGMs with direct joining may lead to large residual stress from dissimilar materials. Therefore, FGMs with a compositional gradient between two materials have been designed to resolve or at least minimize this problem [8,9].

Nickel-based alloys have been widely used in engineering applications because of their high-temperature service potential and their corrosion resistance [10]. Titanium-based alloys are more attractive for aerospace applications due to their low density and high resistance to creep and oxidation resistance at evaluated temperatures [11]. The multi-materials of Ni-based alloys to Ti-based alloys are expected to find use in aerospace applications, which can increase the maximum working temperature and reduce weight. Nevertheless, bonding these materials is very challenging. Recently, some researchers studied TiNi-based graded materials. They prepared a Ti6Al4V/Inconel625 gradient coating by laser melting deposition (LMD) [12] and directed energy deposition (DED) [13] processes while also studying the change in alloy composition and structure. The phase composition of the gradient zone changes according to the formation of the brittle phases (Ti_2Ni, $CrNi_2$), which affect cracking in the gradient transition layer region. The joining of Ni-based alloys and Ti-based alloys is extremely difficult owing to the lack of metallurgical compatibility between these two materials, such as their different physical properties and chemical compositions along with the high reactivity between Ni and Ti [14]. Most researchers prefer to use the LMD and DED processes to fabricate FGMs because of the ease of combining compositional graded on each layer. However, it is possible to manufacture FGMs by the L-PBF process and L-PBF has several advantages over DED, such as higher resolution using thinner and smaller laser diameter and less need for a support structure. Thus, it is more appropriate to build complex geometries using L-PBF rather than DED. So far, the study on the joining of Ni to Ti is rather insufficient, especially for FGMs with compositional gradient paths prepared by the L-PBF process.

In this present investigation, we examine the deposition of a graded binary Ni–Ti alloy via L-PBF starting from a powder feedstock composed of a blend of elemental Ni and Ti powders. Microstructure evolution along the build direction behavior is analyzed, including elemental composition, microstructure, and phase composition together with mechanical properties. The objectives of this work are to obtain preliminary knowledge and data on graded materials using layer-by-layer L-PBF additive manufacturing to improve and develop both the understanding and the design of other multi-materials.

2. Experimental procedure

Functionally graded materials (FGMs) Ni–Ti alloy were fabricated by a laser powder bed fusion process (SLM 280HL: SLM Solutions, Germany) under an argon atmosphere. The particle sizes of the Ni and Ti powders used to build the FGMs ranged from 10 to 45 μm. This deposition system can deposit two different powders during fabrication and allows for the volumetric fraction of Ni and Ti powders to be varied by about 10% per deposited layer. In this work, the FGMs were built from pure Ni to pure Ti, with a 10% decrease in Ni and a 10% increase in Ti in 10 steps. Each of the compositions was deposited in 50 layers. The machine is equipped with two powder feeders, allowing two distinct metal powders to be individually supplied, mixed, and concomitantly deposited. Argon gas was used as a carrying gas to deliver the powder from the hopper through the pipeline to the main container and to the powder container in the chamber. A gradient in composition along the build direction was attained by changing the flow rate of the powders to the powder container. A schematic diagram of the L-PBF system with two powder feeders is shown in Fig. 1(a). In this fabrication, a cylindrical sample 10 mm in diameter and 16.5 mm tall was built using a 1060 nm Yb:YAG, operated at a scanning speed of 1200 mm/s, a layer thickness of 30 μm, and hatch spacing of 80 μm with a scan pattern of 90° between layers, as shown in Fig. 1(b). For laser power, 210 W (energy density = 73 J/mm^3) was applied to the deposit from pure Ni until the 0.7Ni:0.3Ti regions, at which point it was changed to 120 W (energy density = 41.6 J/mm^3) because the problems associated with local overheating were observed after adding Ti content more than 30 at% until the deposition was completed.

The cylinder sample was cut vertically with a wire cutting machine such that the cross-sectional surface of the gradient sample could be mounted, ground, and polished for characterization. The microstructure and chemical composition of the sample were studied using a scanning electron microscope (SEM; JSM-6010 LA, JEOL) with energy-dispersive X-ray spectroscopy (EDS) operating at 20 kV. A micro-X-ray diffraction was performed to analyze the phase compositions of different regions through the build direction (SmartLap; Rigaku). The Cu-Kα radiation generated by a rotating anode with acceleration voltage and current of 45 kV and 200 mA, respectively, was used as the incident X-ray, and the diffracted X-ray was detected by a HyPix-3000 pixel array detector with a scan speed of 4°/min in the range of 10-140°. The obtained diffraction image was converted the XRD profile with a step size of 0.02°. To reduce the X-ray beam diameter to 500 μm, a pinhole collimator was used. The same sample observed SEM/EDS (with supported by conductive resin) was mounted on the moveable XY stage to analyze the selection region, with each region having a distance of 1 mm along the

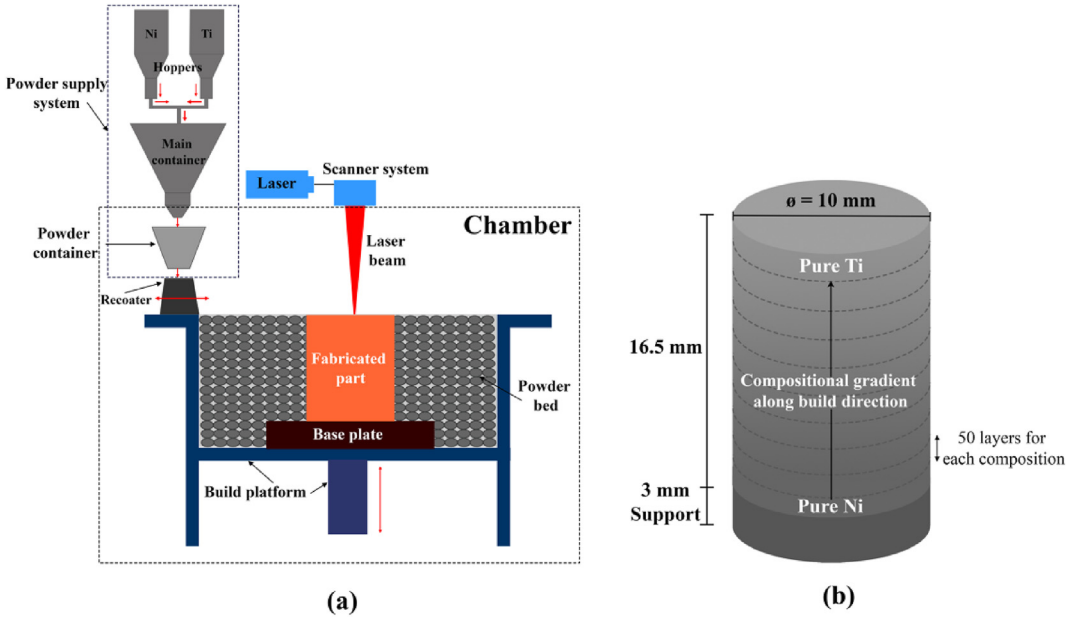

Fig. 1 – Schematic diagram of (a) the laser-powder bed fusion (L-PBF) device equipped with two feeders and (b) the detailed FGM graded from a Ni to Ti sample.

build direction from Ni region to Ti region. In addition, microstructure and additional phase analyses were performed by electron backscatter diffraction (EBSD), using a JSM-7001F (JEOL) microscope operating at 20 kV.

The crack density (η) of the sample was determined by SEM measurements. The crack density in each region through the compositional gradient was analyzed from at least 5 images per region of BSE images at 100× magnification. ImageJ was used to the measure the crack length of each region. A theoretical calculation of the crack density measurement from two-dimensional cracks, according to Budiansky&O'Connell 1967 [15], is

$$\eta = \frac{8}{\pi^3} M \cdot (l)^2 \quad (1)$$

$$M = \frac{n}{h \times w} \quad (2)$$

Where l = the average length of the cracks (μm), M = the total crack number per unit area (number/μm^2) in an SEM image with equation (2), n = the crack number, and h and w = height (μm) and width (μm) of the image, respectively.

The average hardness of each region along the build direction was examined by a Vickers hardness tester (AMT-7FS; Matsuzawa) with a load of 200 g and a dwell time of 15 s. The hardness was randomly measured from 5 points per region across the compositional gradient to obtain an average cross-sectional value.

A computational study of phases was performed using the Scheil simulation model. The FGMs Ni–Ti system was analyzed using Thermo-Calc software in order to predict the equilibrium phase relations and the results of microstructural analyses across the entire compositional gradient. Even though AM process is a non-equilibrium process, performing these phase equilibrium calculations at multiple temperatures and estimating the compositional gradient can explain the phase evolution in the FGM during deposition by a non-equilibrium process.

3. Results

3.1. Computational results

The CALPHAD model was used to explain the phase transformation, especially intermetallic phases that appeared during fabrication as a function of position in the gradient. There are two intermetallic phases and NiTi solid solution phases that were predicted in the equilibrium binary Ni–Ti phase diagram, as shown in Fig. 2. Both intermetallic phases including Ni_3Ti and $NiTi_2$ were predicted to precipitate at equilibrium. In addition, the BCC_B2 phase was presented as NiTi solid solution. The equilibrium phase diagram also presented the primary FCC-Ni and HCP-Ti (α-Ti) together with BCC-B2#2 (β-Ti) at the Ni and Ti sides, respectively.

At 1123 K from pure Ni to pure Ti, the thermodynamic calculation predicts first the only FCC-Ni solid solution phase followed by the Ni_3Ti intermetallic phase (Fig. 3). After 8 vol% Ti, the Ni_3Ti begins to precipitate and to disappear in order to form $NiTi_2$ intermetallic nearby 45vol%Ti in the calculation. The $NiTi_2$ appeared beginning at 45vol% until 90vol%Ti, which it was influenced by the proportion of Ti. Apart from the intermetallic phases, the NiTi B2 (BCC_B2) solid solution begins forming at more than 20vol%Ti and peaks at around 45vol%Ti, which is close to the composition ratio of NiTi shape memory alloy [16,17] and also was predicted again at close to pure Ti.

3.2. Microstructure

Atomic percent measurements were analyzed on a cross-sectional of the sample, starting from the bottom of the

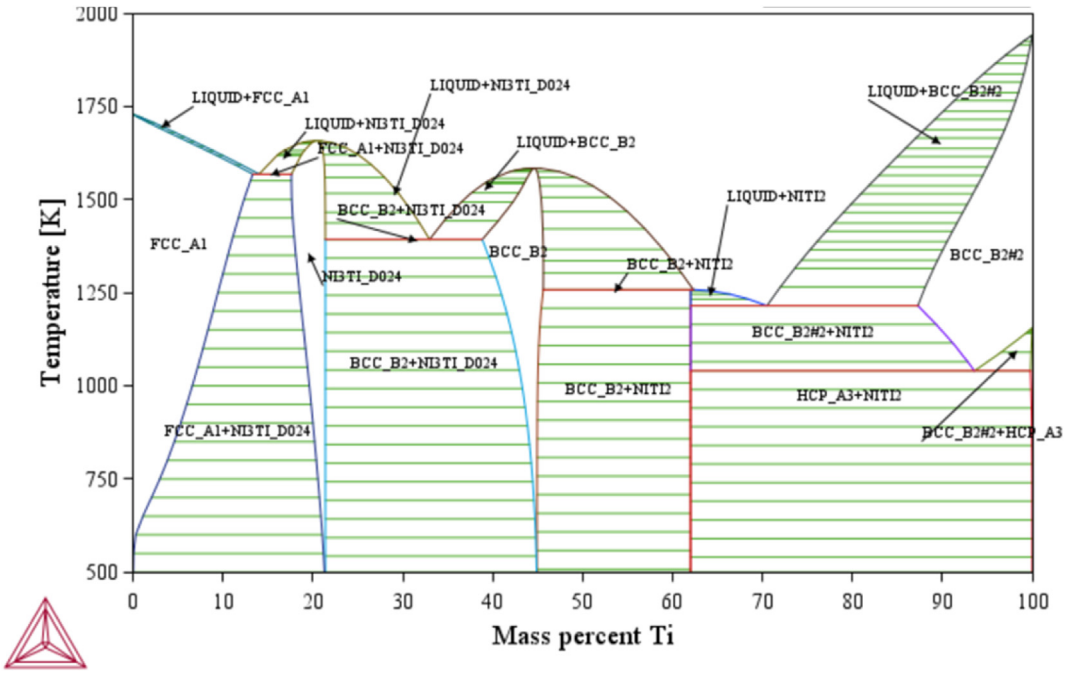

Fig. 2 – Phase equilibria computed form TCTI3 database of Ni–Ti system.

sample (Ni side) to the top of the sample (Ti side), as shown in Fig. 4. The result shows that Ni content declines steadily, whereases the Ti content becomes increases sharply. The EDS (at%) profile qualitatively manifests that a smooth gradient proportion transition of Ni and Ti was found in the build direction. This demonstrates the successful fabrication of the compositional gradient part by L-PBF process with two powder hoppers, according to the designed composition. The detailed microstructures of the sample can be approximately divided into 11 distinct regions following the change in the Ni and Ti contents controlled by the powder feeder in L-PBF, as presented in Fig. 5. Backscatter electron (BSE) images and EDS

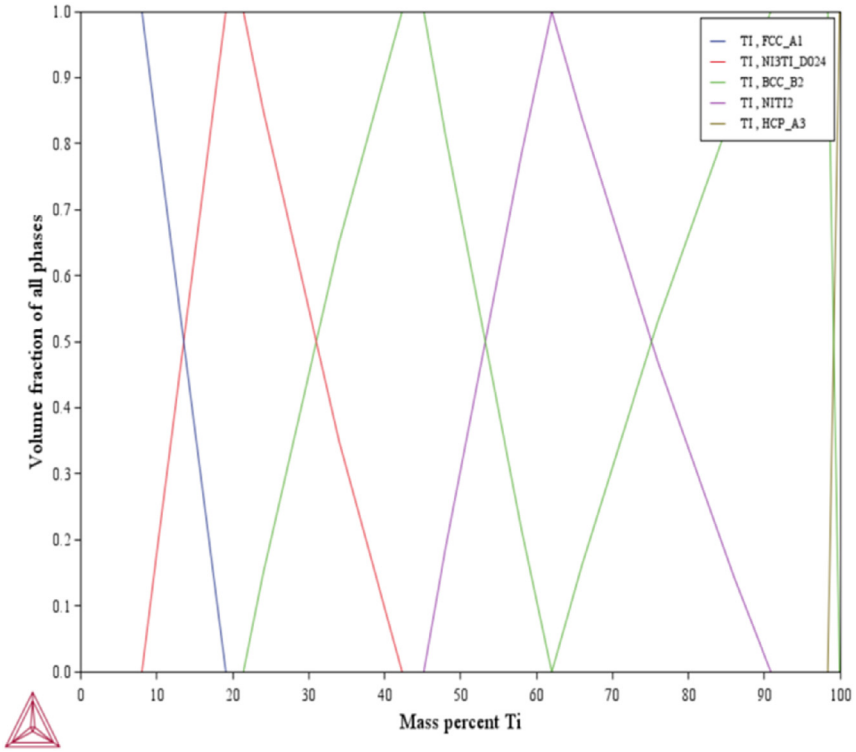

Fig. 3 – Phase fraction as predicted by CALPHAD modeling at 1123 K along the vertical section from pure Ni to Pure Ti. This temperature was selected because of its falls below the solidus line.

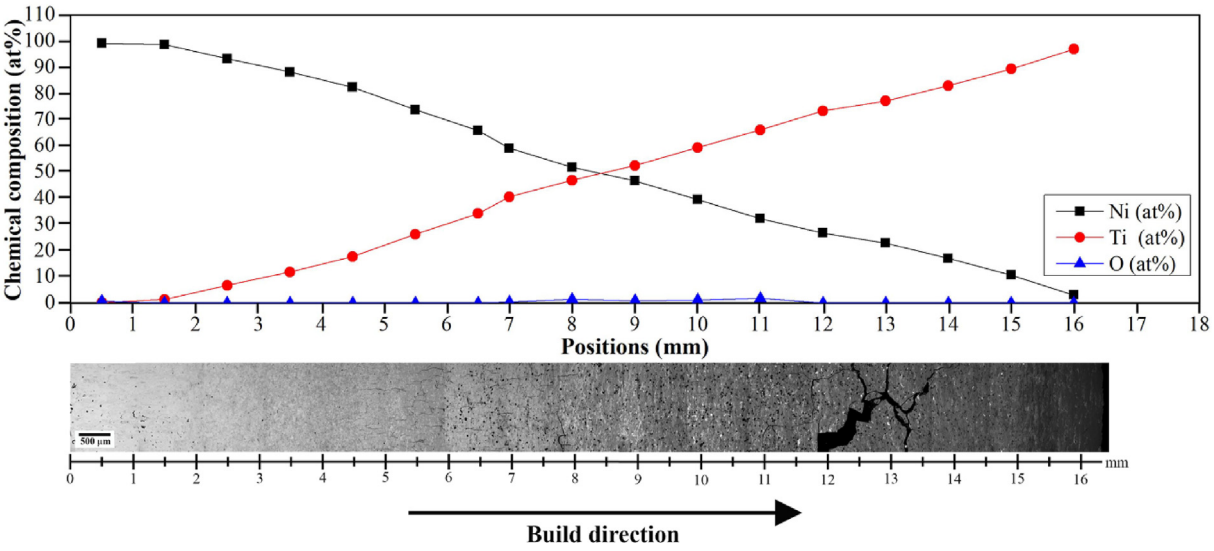

Fig. 4 – Plot of the composition profile across the L-PBF deposited FGMs Ni–Ti alloys.

maps for the FGMs Ni–Ti present the microstructural change and elemental distribution for Ni and Ti elements across the build direction. Vertical cracks were found at the centers of the FGMs, which were related to the change in the Ni and Ti ratio. The melt pools in the pure Ni region are visible in the BSE image in Fig. 6(a), with columnar grains that grow and elongate in the build direction. When of Ti content was added, the microstructures were refined. The melt pool was half-cylindrical and shallow. Moreover, the equiaxed grain zone extends to the center of the melt pool, and the melt pool boundary is packed with fine columnar grains, as seen in the 10-20 at%Ti regions in Fig. 6(b and c). Nevertheless, the proportion of Ti added up to 30 at% (Fig. 6(d)), and a columnar dendrite dominating mostly the microstructure along with an equiaxed dendrite were found in this region.

With increasing Ti content up to 40 at% onward, the laser power was changed from 210 W to 120 W. The melt tracks showed a curved and wavy morphology, with irregular

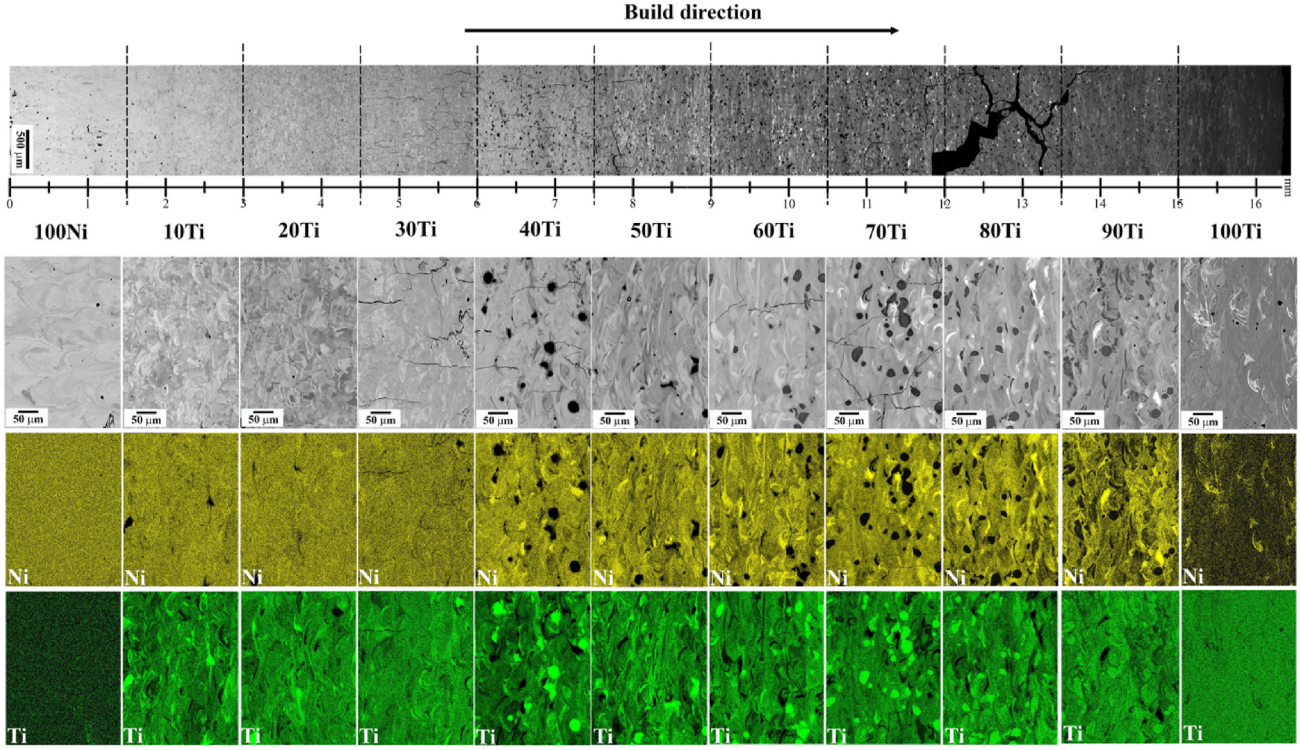

Fig. 5 – BSE and EDS maps of FGMs NiTi showing the microstructural change and elemental distribution for Ni and Ti elements. The microstructures of 11 regions are shown microstructure along compositional graded built by changing the chemical composition from pure Ni (left) to pure Ti (right).

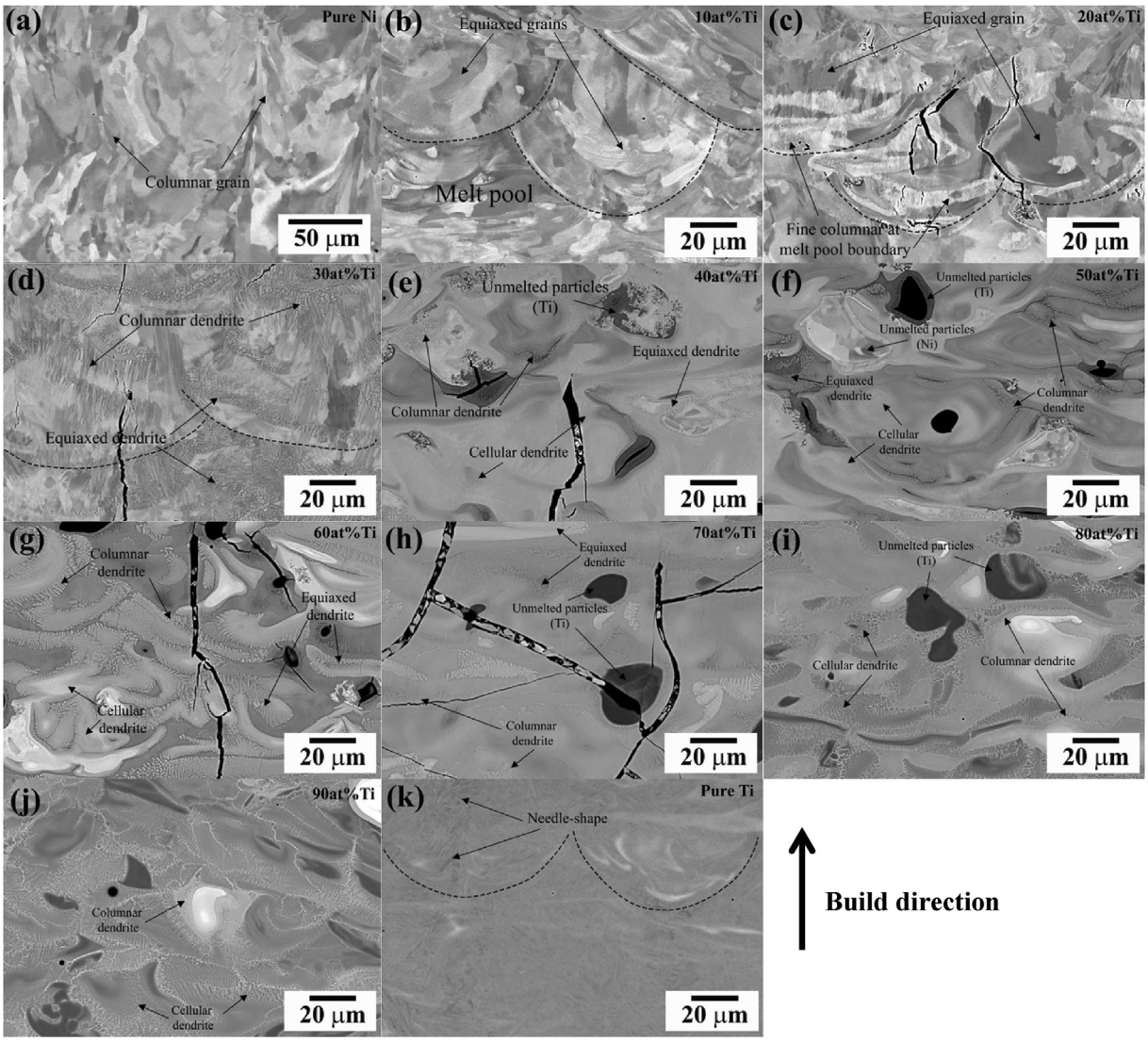

Fig. 6 – BSE images of the detailed microstructure of each region with a different composition on the FGMs Ni–Ti sample.

overlap and variation between adjacent layers. In addition, unmelted particles of Ti (black contrast) and Ni (white contrast) were found and distributed in these regions (Fig. 6(e–j)). The result shows microsegregation in the melt pool, which evolves into a cellular dendritic microstructure. Moreover, a superfine equiaxed dendrite and a columnar dendrite were observed inside the melt pool. Finally, the microstructure of pure Ti in Fig. 6(k), comprised of very fine needle-shaped microstructures can be seen in the melt pool.

3.3. *Cracks morphology*

Fig. 7 shows the overall forming morphology of the FGMs Ni–Ti sample using L-PBP process. Two macro horizontal cracks were found in the regions containing 40 and 70 at%Ti contents, respectively. Fig. 8 shows the crack length and crack density of FGMs NiTi through the build direction. The result shows that cracking initiated in the region that consisted of approximately 20 at%Ti. The crack density was likely to continue increasing and rose to a high value, peaking in the 30 at%Ti region until the sample cracked in half vertically in the region composed of 40 at%Ti content. The SEM image at the 20 at%Ti regions shows the presence of microcracks surrounded by the area composed of 24.5 at%Ti concentration at the melt pool boundary. Similarly, the chemical composition of the columnar dendrite area in the 30 at%Ti region also consists of a 25 at%Ti concentration. EDS analysis was carried out in both areas, revealing the same composition, which induced the expansion of cracking until failure in the 40 at%Ti region. After that, there are no cracks in 50 at%Ti regions. However, cracking was observed again in the 60 at%Ti region and there rose steadily until the sample broke in half vertically in the 70 at%Ti. As the SEM image of the 60 at%Ti region shows, microcracks first start to nucleate in the area containing ~69 at%Ti concentration by EDS. The result of EDS analysis from both areas, consisting of ~24.5 at%Ti and ~69 at %Ti concentrations, can assume that these areas are Ni_3Ti and $NiTi_2$ intermetallic phases, respectively, which similar to the composition as reported by Jun.et al. [18].

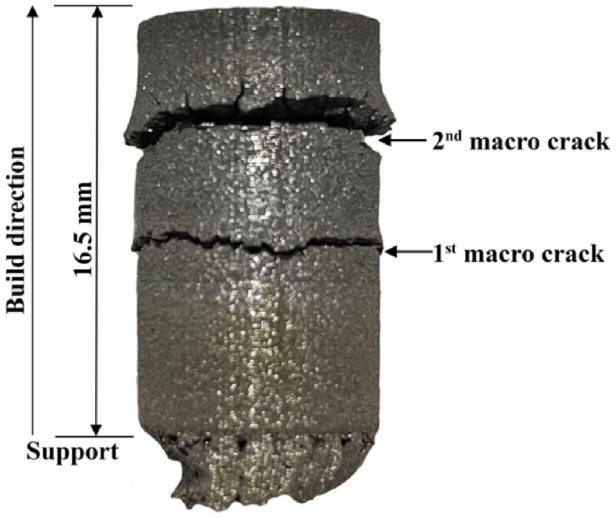

Fig. 7 – Photograph and schematic of the FGM sample graded from Ni to Ti, with alloying given in at% and the apparent locations of the two macroscopic cracks.

3.4. *Phase compositions*

The different compositions of Ni and Ti elements have significantly influenced on the phase formations and fractions in different regions. Micro-XRD was used to experimentally determine the presence of different phases throughout the transition region. Fig. 9 shows the XRD patterns of a whole sample along the compositional transition range from position 1 (0.2 at%Ti; bottom) up to position 17 (97 at%Ti; top), with phase fraction data given in Table 1. Together, the figure and table show a tendency toward phase formation for FGMs Ni–Ti alloy. The main component in the Ni side (points 1–3) is FCC-Ni, while that in the Ti side (point 17) indicates the presence of α-Ti phase. With the addition of Ti and layers added, the different composition ratio between Ni and Ti throughout the build direction leads to complicated phase formations, which indicates the presence of intermetallic compounds and NiTi solid solutions. A series of phase transformations took place along the sample: FCC-Ni → FCC-Ni + Ni_3Ti → Ni_3Ti + NiTi (B2, B19', R phase) → NiTi (B2, B19', R phase) + $NiTi_2$ → $NiTi_2$ + β-Ti + α-Ti → α-Ti. With increasing Ti content up to 12 at% exists in two phase γ + Ni_3Ti (Table 1), which the volume fraction of Ni_3Ti tend to increase until reaches the peak at 26 at%Ti. In the phase fraction for 26 at% Ti, there is a significant amount (65vol%) of the Ni_3Ti, with 29vol% of γ-Ni solid solution, corresponding to the SEM image in the 30 at%Ti region where crack density peaks. After that, the volume fraction of Ni_3Ti gradually decrease, while that of NiTi solid solution (B2, B19', R phase) and $NiTi_2$ increase. The main phases of the regions containing 50 at%Ti onwards are NiTi solid solution and $NiTi_2$. The ~70 at%Ti region has a higher volume fraction of 40–43vol% $NiTi_2$ compared to other regions, which also show peak crack density. The increasing of crack density in the FGMs NiTi is attributable significantly to the formation of intermetallic compounds (Ni_3Ti and $NiTi_2$).

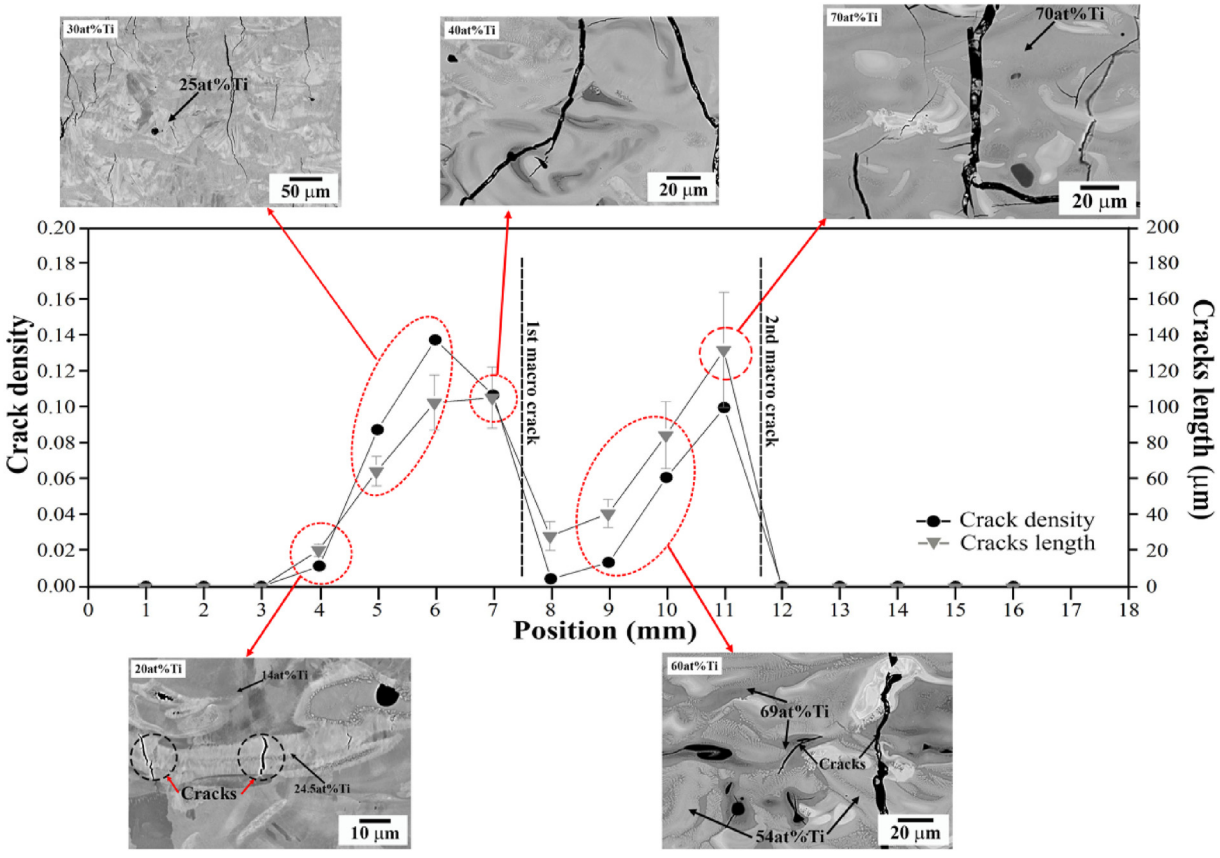

Fig. 8 – Crack density and length profiles of the FGMs Ni–Ti sample along the build direction.

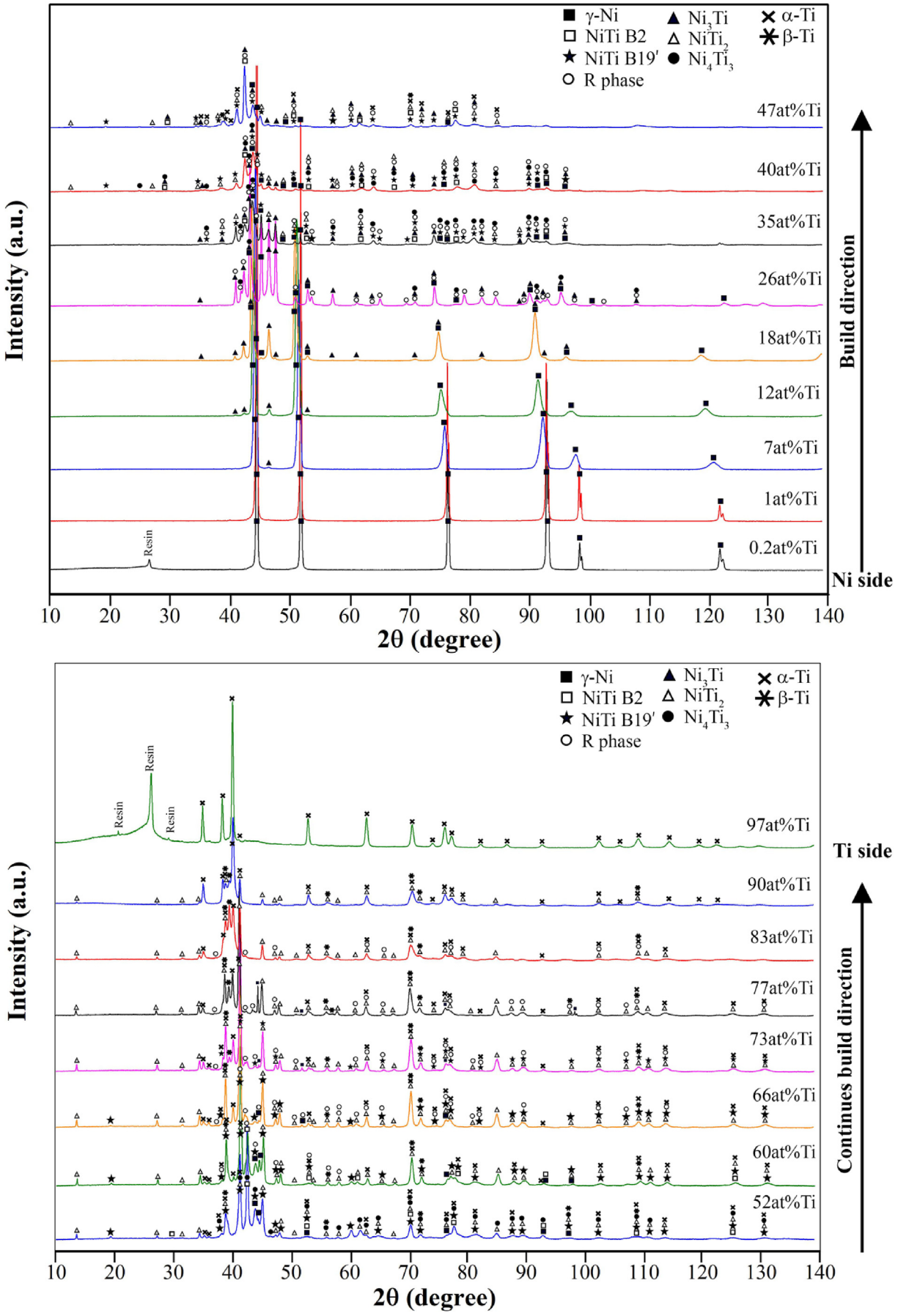

Fig. 9 – XRD patterns as a function of position from the pure Ni region to the pure Ti region along the build direction.

Table 1 – Volume fraction of phases through build direction identified by micro-XRD analysis, according to Fig. 9

Position	Ti (at%) by EDS	Phase fraction (vol%)								
		FCC Ni	NiTi B2	NiTi B19′	NiTi R phase	Ni_3Ti	$NiTi_2$	Ni_4Ti_3	α-Ti	β-Ti
1	0.2	100	–	–	–	–	–	–	–	–
2	1	100	–	–	–	–	–	–	–	–
3	7	100	–	–	–	–	–	–	–	–
4	12	97.86	–	–	–	2.14	–	–	–	–
5	18	86.3	–	–	–	14	–	–	–	–
6	26	29	–	–	0.03	65	–	5.2	–	–
7	35	16.4	12.4	24.4	0.22	43	0.38	3	–	–
8	40	26.7	51	17.6	0.2	2	6.4	2	–	–
9	47	1.09	49	31	0.1	1.6	7	–	8.1	2
10	52	10	26	43	–	–	10.7	7	2.1	1.8
11	60	3.9	29	17	0.2	–	31	–	8	7
12	66	1.6	1.01	12.7	0.9	–	38	–	27.9	10
13	73	1.8	–	5	8.6	–	40	–	28	18
14	77	0.7	–	–	2.3	–	43	–	40	7.7
15	83	–	0.77	–	–	–	21	–	57	21.2
16	90	–	–	–	–	–	7.4	–	85.6	6.8
17	97	–	–	–	–	–	–	–	100	–

In order to explain the crack propagation of each region in relationship to phase formation, the amount of intermetallic compounds present must be determined. Figs. 10–12 present the EBSD results of the regions before the first and second horizontal macrocracks occur, respectively. EBSD IPF + IQ and phase maps of two regions, including pure Ni and 10 at%Ti regions, were acquired, as shown in Fig. 10. The IPF + IQ map of the pure Ni region exhibits a tendency toward only γ-Ni columnar grains to grow along the build direction. After the addition of 10 at%Ti, the microstructure changed from columnar grains into equiaxed grains. The EBSD phase map is composed mainly of FCC-Ni and a small amount of Ni_3Ti phase. Likewise, a larger amount of Ni_3Ti appeared, and vertical microcracks were found at the melt pool boundary in the

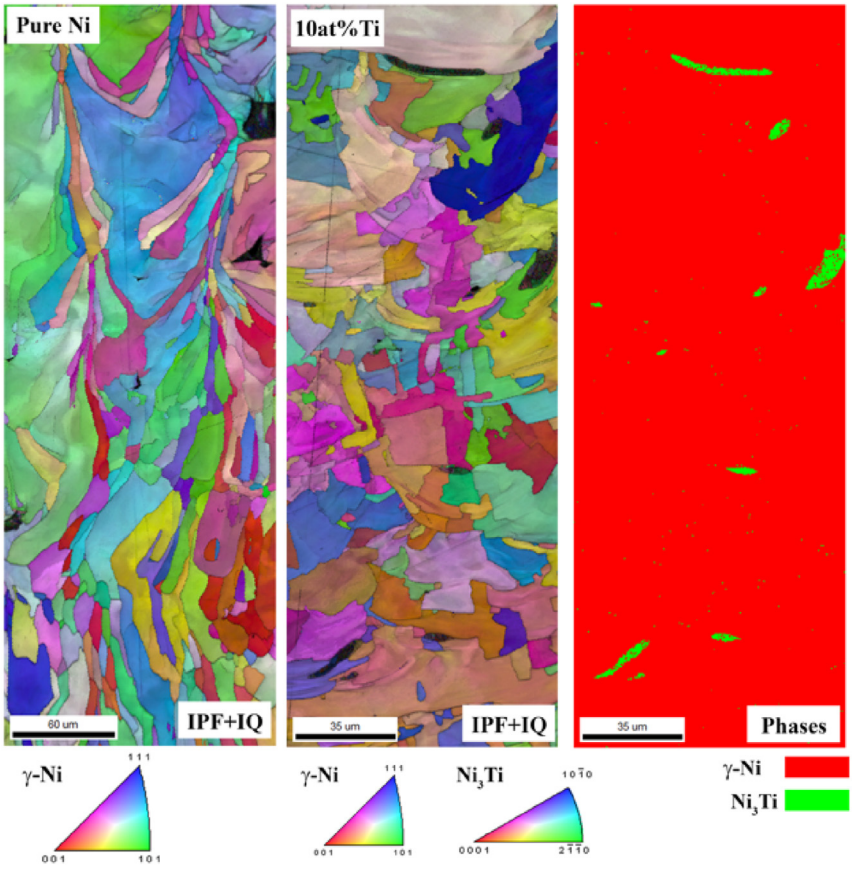

Fig. 10 – EBSD images show the image quality (IQ) + inverse pole figure (IPF) maps and EBSD phase maps of the pure Ni and 10 at%Ti regions. No cracks were observed in these regions.

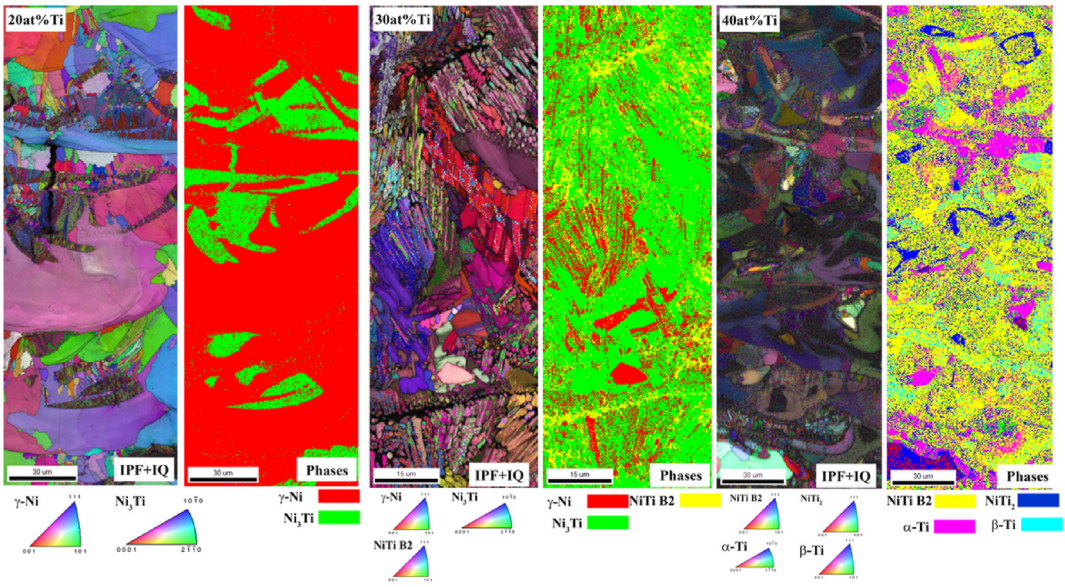

Fig. 11 – EBSD images show the image quality (IQ) + inverse pole figure (IPF) maps and EBSD phase maps of 20–40 at%Ti regions. Cracks were observed in these regions before the first horizontal macrocrack occurred.

20 at%Ti region (Fig. 11). EBSD results confirmed that cracks seem to be initiated at the melt pool boundary, where the fine grain is clear and a part of acicular Ni_3Ti precipitated. At 30 at %Ti regions, a columnar dendrite solidification structure within melted tracks was appeared. The columnar dendrite is clearly seen in the full of Ni_3Ti phase (green color), while NiTi B2 solid solution phase (yellow color) was formed in the interdendritic. The changing from γ-Ni to Ni_3Ti of the main phase would be increase the brittleness and expand the cracking in this region. However, the Ni_3Ti phase was disappeared and the NiTi B2 phase was distributed together with small amounts of $NiTi_2$, α-Ti, and β-Ti in the 40 at%Ti region. While the proportion of Ti reaches more than 50 at%, these regions consist of very fine grains of NiTi B2, with columnar grains of retained $NiTi_2$ forming between them, as shown in Fig. 12. Compared to the region containing less than 50 at%Ti content, the EBSD phase maps identified $NiTi_2$, where cracks initiated and then expanded to the NiTi B2 phase area, as seen in Fig. 12(a). The increase in the $NiTi_2$ area is key factor for increased crack length and connected cracking, leading to

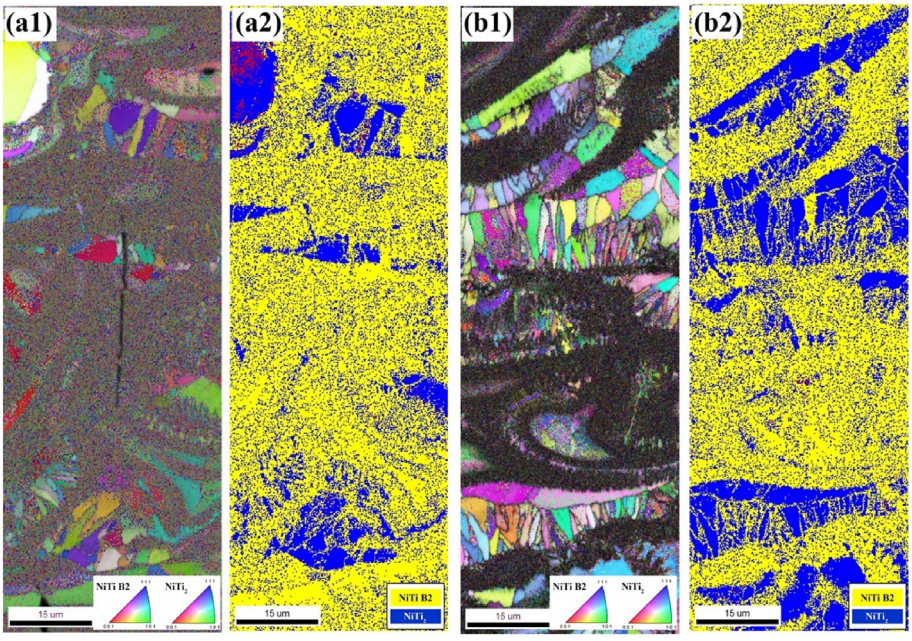

Fig. 12 – EBSD images showing (a) 60 at%Ti and (b) 70 at%Ti regions, where (1) shows the image quality (IQ) + inverse pole figure (IPF) maps and (2) shows EBSD phase maps. Cracks were observed again in these regions before the second horizontal macrocrack occurred.

the second horizontal macrocrack in the FGMs NiTi. The appearance and amount of phase formation on each region from the EBSD results corresponded to the XRD results.

3.5. *Hardness distribution*

Vickers hardness measurements were taken along the build direction for the whole sample (Fig. 13). The pure Ni region has the lowest hardness value, approximately 120 HV, whereas the hardness value of the pure Ti region was ~290 HV. Obviously, the hardness profile begins raising gradually with the increment of Ti content until the ~30 at%Ti region, resulting in peak hardness (~685 HV). As the composition ratio changes, the Ti content increases, and Ni_3Ti intermetallic compound is generated gradually, according to the phase fraction in the XRD result, resulting in the increase in the hardness value. According to the mechanical properties of the intermetallic compounds in the Ni–Ti system, the Ni_3Ti phase has a much higher hardness value than the other phases [19]. The hardness value then drops slightly when the Ti content reaches 50 at%. As it can be noticed, the decrease in the volume fraction of Ni_3Ti in the component with 40–50 at%Ti regions also results in a big difference in the hardness of these regions, with a gradual decrease from 685 HV to 350 HV. Nevertheless, the hardness values tend to increase again at the 60 at%Ti region and have an almost constantly in the high Ti content, with an average value of ~520 HV. This is due to the fact that the main phases of these regions are $NiTi_2$ and NiTi B2, and the hardness values of the two phases were lower than those of Ni_3Ti phases.

4. Discussions

4.1. *Microstructure evolution*

The microstructural and phase evolutions of FGMs NiTi are based on the compositional gradient along the build direction together with the high cooling rate during the L-PFB solidification process, indicating the generation of an inhomogeneous microstructure. According to the experimental results, phase formation after the adding of 13 at%Ti onward can be understood in a similar the compositional result. The thermodynamic calculation assesses that the Ni_3Ti phase initially forms in liquid phase. The Gibbs free energy for Ni_3Ti (−117.8 kJ/mol) is lower than those for the other intermetallic compounds (−78.7 kJ/mol for $NiTi_2$ and -58.2 kJ/mol for NiTi) in this system [17], which preference for the formation of this phase over the other phases at the region containing <50 at% Ti concentration. When the Ni and Ti powders are melted and mixed by the laser, lots of Ni_3Ti precipitates formed first at the edge of the melt pool and columnar crystals continue to grow during solidification. Then, the solute of liquid phase at the tip of the columnar dendrite was changed, leading to the appearance of a lot of fine γ-Ni equiaxed crystal. The equiaxed γ-Ni continues to growth at the center of the melt pool. At the end of solidification, fine Ni_3Ti columnar grains can be seen at the edge of the melt pool and appear to be the γ-Ni equiaxed grain at the center of melt pool, as shown in the solidification diagram on Fig. 14 (a). At the 30 at%Ti region, increasing the Ti content tends to increase columnar dendrite Ni_3Ti intermetallic phase, which is the main phase of this region. Similar to the solidification mechanism on previous regions, the primary Ni_3Ti dendrite arm starts to solidify and then grows inside the melt pool under high rate of solidification. After that, NiTi (γ-Ni and B2) solid solution forms at interdendritic regions, which is the final phase solidification. Apart from the different composition of each phase, the effect of thermal gradient (G) and solidification rate (R) is one of factor to indicate the grain morphology and size. During solidification, the high G/R ratio at melt pool boundary leads to the solidification microstructure grows in planar or cellular, but the rapid cooling and high solute is greater than the equilibrium solidification, resulting to the higher crystallization rate at the edge of melt pool [20,21], It can be seen the fine-grained at melt pool boundary in the microstructure after adding Ti content. After that, columnar grains grow epitaxially from the melt pool boundary through the center of the melt pool along with slightly decreased G/R ratio. At low thermal gradient (G) and low solidification rate (R) at top of melt pool, the number of equiaxed grain seems to increase, and then the grain morphology changes from columnar dendritic to equiaxed crystal, as shown in Fig. 14(b).

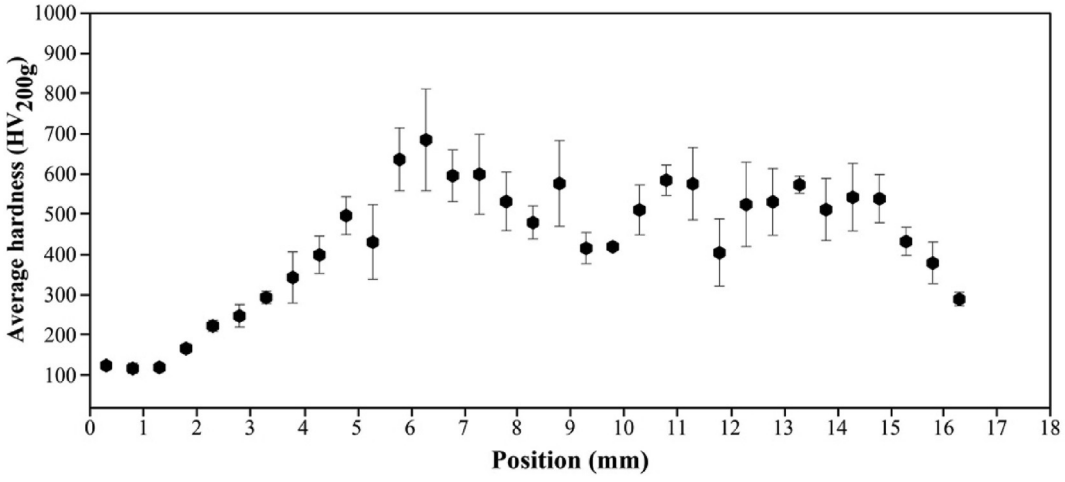

Fig. 13 – Hardness profile of the FGMs Ni–Ti sample, measured across the build direction.

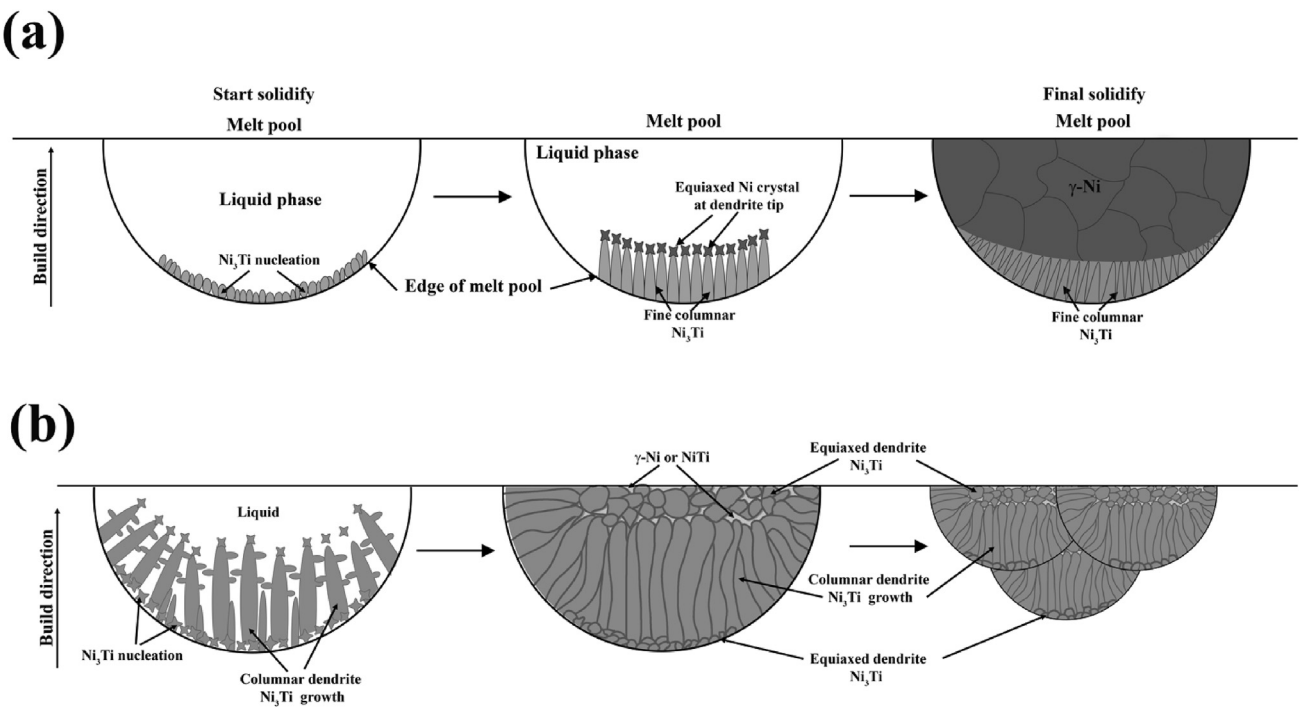

Fig. 14 – Schematic diagram of solidification mechanism of the melt pool on regions containing (a) 10-20 at%Ti and (b) 30 at %Ti.

Nevertheless, the decrease in energy density and the increase in Ti content together exert a powerful effect upon microstructure and phase composition through the 40 at%Ti-deposited region onward. When more than 40 at%Ti is added, the liquid temperature tends to fall, according to phase diagram (Fig. 2). This is due to the fact that the rate of heat accumulation in these regions increases with increasing height because the mixed Ni and Ti regions have lower thermal conductivity than the Ni region, resulting in a decreased the liquidus temperature. In addition, the great differences in thermophysical properties between Ni and Ti requires a different L-PBF process parameter. Even though the melting point of Ti (1668 °C) is higher than that of Ni (1446 °C), the thermal conductivity of Ti is very low (16.3 W/mK for Ti and 67.5 W/mK) [22], thus making is possible to use the low laser energy to fully melted powders. However, the unmelted particles at some places remain, which means that the amount of energy (41.3 J/mm^3) supplied to the power bed is not enough to melt the powder bed completely. Moreover, finer cellular, equiaxed, and columnar structures were observed, which caused by the higher temperature gradient and cooling rate. The main phase composition was completely changed from the Ni_3Ti to the NiTi B2 and $NiTi_2$ phases. The phase compositions of NiTi B2 and $NiTi_2$ are explained in the following equilibrium phase fractions (Figs. 2–3). As the Ti content continues to increses, the peak of NiTi B2 was reportedly prone to appear when Ti reached to 40 at% at the same time, $NiTi_2$ started to precipitate. In addition, the volume fraction of $NiTi_2$ rises first and then decreases. During solidification, NiTi nucleates and grow in the edge of the melt pool. $NiTi_2$ crystal forms to surrounding the NiTi at favorable locations and solidifies with the growth of NiTi and $NiTi_2$. The NiTi phase surrounded by the $NiTi_2$ phase is similar to that reported by Gao et al. [23]. The limitation of Ti diffused into NiTi leads to the segregation of Ti to interdendritic spaces and forms $NiTi_2$ intermetallic compound. Apart from the NiTi B2 phase, the diffraction peaks corresponding to the B19′ and R phases appear in the XRD pattern of 35–77 at%Ti regions. The martensitic transformation (B2–B19′-R) was expected to occur even in rapid solidification of the Ni–Ti alloy [24]. The martensitic transformation would act very quickly in response to the thermal change. When Ti content approached pure Ti, the $NiTi_2$ and NiTi phases disappeared gradually, and the complete stabilization phase of the β-Ti and α-Ti phases was found in the 90-100 at%Ti regions. The appearing of β-Ti is believed to be due to the fact that Ni is a strong β-stabilizer [25]. The phase diagram shows the possible metastable β-Ti phase in the Ni–Ti system during rapid solidification.

4.2. *Crack propagations*

Cracking was found in the gradient zone along with two horizontal macrocracks found in the regions containing 40 and 70 at%Ti content, respectively. The main factors of the cracking in the FGMs Ni–Ti sample are explained by (i) the precipitation of various phases and (ii) thermal and residual stress by cyclic heating and rapid cooling [26]. Therefore, the component ratios of Ti with 20 and 30% clearly show the Ni_3Ti phase as the brittle phase in the Ni–Ti system. Cracks were found in an area where there are more Ni_3Ti precipitates. Ni_3Ti is much stronger than NiTi solid solution, and their thermal expansion rates and crystal structures also differ between them. So, crack initiation mostly nucleates on the Ni_3Ti phase as a brittle phase rather than a ductility phase (NiTi). In

addition, Ni_3Ti tends to increase with increasing Ti content, resulting in crack elongation in regions containing 30 at%Ti. Apart from the brittle phase, the large residual stress and the stress concentration from cyclic heating and rapid cooling are driving forces when cracks expand and connect to other cracks, resulting in horizontal macrocracking in the next region. In the same way, the $NiTi_2$ phase is the main factor in initiating the cracks propagation in the 60 at%Ti region. The difference in solidification temperature between dendrite NiTi and interdendrite $NiTi_2$ induces stress during solidification. The dendrite NiTi remains in the solid state, whereas the $NiTi_2$ transforms into an interdendritic liquid film, leading to a shrinkage between the solid and liquid phases. When the stress relieves the tensile limit, the liquid film is pulled apart, and cracking is generated. The cracking in the FGMs Ni–Ti alloy is similar to that in another reports [27] that presented macrocracks in the 30–70%Inconel625/Ti6Al4V prepared by laser melting deposition due to the brittle phase precipitated by an increase in the proportion of nickel-based alloy. The various phases in the FGMs Ni–Ti sample, especially in the gradient zone, have differences in melting point, yield strength, crystal structure or thermal expansion, and residual and thermal stress; these different were induced to initiate cracks at stress concentrations within the gradient zone. The FGMs Ni–Ti sample had a multi-phase region with a solid solution and intermetallic phases.

4.3. *Effects of microstructure and phase on hardness values*

In this study, the hardness value of the gradient zone is much higher than that of either the pure Ni or Ti regions in the FGMs Ni–Ti sample prepared by L-PBF process. It can be assumed that the strong hardness contribution of the gradient zone depended largely on the brittle phases (Ni_3Ti and $NiTi_2$). Moreover, the rapid cooling in L-PBF process creates the fine grain in the FGMs sample. The fine grain with intermetallic phases can further enhance the grain refinement and dislocation accumulation effect, which is a factor to improving the hardness of FGMs. Nevertheless, the hardness value is negatively correlated with the crack density; this negative correlation is attributed mainly to the fact that the effect of brittle phases precipitate, as explained in previous sections.

5. Conclusions

This work presented a new strategy to fabricate the FGMs Ni–Ti with compositions ranging in steps of 10 at% from pure Ni to pure Ti using the L-PBF process. The following results were obtained.

1. The microstructure and phases composition change with increase in Ti content. In the gradient zone, columnar dendrites and equiaxed dendrites are sequentially distributed through the gradient zone because of the different on composition ratio and G/R ratio during solidification. According to CALPHAD, the experimental microstructure and elemental analysis of the binary Ni–Ti shows that phase transformation may happen under a different composition ratio across the build direction. The phase constitution varies depending on Ni and Ti ratio, the functional graded material changes as follows: $\gamma \rightarrow \gamma + Ni_3Ti \rightarrow Ni_3Ti + NiTi\ B2 \rightarrow NiTi\ B2 + NiTi_2 \rightarrow NiTi_2 + \beta\text{-}Ti + \beta\text{-}Ti \rightarrow \alpha\text{-}Ti + \beta\text{-}Ti$.
2. The increases in the crack density and hardness value after the addition of Ti content can be explained by the formation of the fine brittle phases (Ni_3Ti and $NiTi_2$) and by the fact that the stress concentration caused by cyclic heating and rapid cooling accelerates the generation and expansion of cracks.

This research illustrates the understanding of microstructure and phase composition together with crack propagation through the build direction of a functionally graded Ni–Ti alloy prepared by L-PBF. This research knowledge can be expanded and used to design a new FGMs or multi-materials of Ni–Ti -based alloy systems along with the development of process parameter to avoid cracking.

Declaration of Competing Interest

The authors declare that they have no known competing financial interests or personal relationships that could have appeared to influence the work reported in this paper.

Acknowledgements

This research work was supported by JSPS KAKENHI Grant Number JP21K03814.

REFERENCES

[1] Vaezi M, Chianrabutra S, Mellor B, Yang S. Multiple material additive manufacturing-part 1: a review, Virtual. Phys Prototy 2013;8:19–50.
[2] Ghanavati R, Naffakh-Moosavy H. Additive manufacturing of functionally graded metallic materials: a review of experimental and numerical studies. J Mater Res Technol 2021;13:1628–64.
[3] Frazier WE. Metal additive manufacturing: a review. J Mater Eng Perform 2014;23:1917–28.
[4] Kim J, Wakai A, Moridi A. Materials and manufacturing renaissance: additive manufacturing of high-entropy alloys. J Mater Res 2021;35:1–21.
[5] Tan C, Zhou K, Kuang T. Selective laser melting of tungsten-copper functionally graded material. Mater Lett 2019;237:328–31.
[6] Chen J, Yang Y, Song C, Wang D, Wu S, Zhang M. Influence mechanism of process parameters on the interfacial characterization of selective laser melting 316L/CuSn10. Mater Sci Eng 2020;792:139316.
[7] Mao S, Zhang DZ, Ren Z, Fu G, Ma X. Effects of process parameters on interfacial characterization and mechanical properties of 316L/CuCrZr functionally graded material by selective laser melting. J Alloys Compd 2022;899:163256.
[8] Sobczak JJ, Drenchev L. Metallic functionally graded materials: a specific class of advanced composites. J Mater Sci Technol 2013;29:297–316.

[9] Hofmann DC, Vecchio KS. Submerged friction stir processing (SFSP): an improved method for creating ultra-fine-grained bulk materials. Mater Sci Eng 2005;402:234–41.
[10] O'Flynn J, Whitman CA, Corbin SF. Thermal property measurements of metal injection moulded Inconel 625 and Inconel 718 using combined thermal analysis techniques. Powder Metall 2020;63:277–87.
[11] Peters M, Kumpfert J, Ward CH, Leyens C. Titanium alloys for aerospace applications. Adv Eng Mater 2003;5:419–27.
[12] Sun Z, Ji X, Zhang W, Chang L, Xie G, Chang H, et al. Microstructure evo- lution and high temperature resistance of Ti6Al4V/Inconel625 gradient coating fabricated by laser melting deposition. Mater Des 2020;191:108644.
[13] Mei W, Yin X, Zhang W, Fang J, Guo L, Ma Q, et al. Additive manufacturing of a functionally graded material from Inconel 625 to Ti6Al4V by laser synchronous preheating. J Mater Process Technol 2020;275:116368.
[14] Chatterjee S, Abinandanan TA, Chattopadhyay K. Microstructure development during dissimilar welding: case of laser welding of Ti with Ni involving intermetallic phase formation. J Mater Sci 2006;41:643–52.
[15] Budiansky B, O'Connell RJ. Elastic moduli of a crack solid. Int J Solid Struct 1976;12:81–97.
[16] Shiva S, Palani IA, Mishra SK, Paul CP, Kukreja LM. Investigations on the influence of composition in the development of Ni-Ti shape memory alloy using laser based additive manufacturing. Opt Laser Technol 2015;69:44–51.
[17] Laeng J, Xiu Z, Xu X, Sun X, Ru H, Liu Y. Phase transformation of Ni-Ti via solid state reaction. Phys Scripta 2007;2007:250.
[18] Jun W, Hu K. Phase transformation of NiTi alloys during vacuum sintering. Mater Sci Eng 2017;204:012023.
[19] Li Y, Tang S, Gao Y, Ma S, Zheng Q, Cheng Y. Mechanical and thermodynamic properties of intermetallic compounds in Ni-Ti system. Int J Mod Phys B 2017;31:1750161.
[20] DebRoy T, Wei HL, Zuback JS, Mukherjee T, Elmer JW, Jo Milewski, et al. Additive manufacturing of metallic components-process, structure and properties. Prog Mater Sci 2018;92:112–224.
[21] Kurz W, Bezencon C, Gäumann M. Columnar to equiaxed transition in solidification process. Sci Technol Adv Mater 2001;2:185–91.
[22] Semboshi S, Takeuchi T, Kaneno Y, Iwase A, Takasugi T. Thermal conductivity of Ni_3(Si,Ti) single-phase alloys. Intermetallics 2018;92:119–25.
[23] Gao S, Feng Y, Wang J, Qin M, Bodunde OP, Liao WH, et al. Molten pool characteristics of a nickel-titanium shape memory alloy for directed energy deposition. Opt Laser Technol 2021;142:107215.
[24] Moon H-Y, Chun S-J, Liu Y, Yang H, Kim Y-W, Nam T-H. Effect of alloy composition on the B2-R transformation in rapidly solidified Ti-Ni alloys. J. Alloys. Comd. 2013;577S:S259–64.
[25] Kolli R, Devaraj A. A review of metastable beta titanium alloys. Metals 2018;7:506.
[26] Zaeh MF, Branner G. Investigations on residual stresses and deformations in selective laser melting. Prod Eng 2010;4:35–45.
[27] Sun Z, Ji X, Zhang W, Chang L, Xie G, Chang H, et al. Microstructure evolution and high temperature resistance of Ti6Al4V/Inconel625 gradient coating fabricated by laser melting deposition. Mater Des 2020;191:108644.